AG-336

7. WALL CORRECTION METHODS FOR POWERED MODELS OF CONVENTIONAL TAKE OFF AND LANDING AIRCRAFT

AUTHORS : J.E. HACKETT (CHAPTERS 7.1, 7.2, 7.4.2 - 7.4.4)
P. R. ASHILL (CHAPTER 7.3)
M. MOKRY (CHAPTERS 7.4.1, APPENDIX)

7 WALL CORRECTION METHODS FOR POWERED MODELS OF CONVENTIONAL TAKE OFF AND LANDING AIRCRAFT

LIST OF SYMBOLS FOR CHAPTER 7 (ADDITIONAL SYMBOLS ARE DEFINED IN CHAPTER 7.4)

A_j	overall cross-sectional area of nacelle nozzle
B	working-section width
C	working-section cross-sectional area
C_{Du} , C_{Lu}	uncorrected drag and lift coefficients
C_{Dtc} , C_{Ltc}	thrust-corrected drag and lift coefficients
C_{Dwb}	drag increment due to wake interference (Figure 7.20)
C_P	pressure coefficient
C_S	spacing between solid blockage source and sink
C_T	net thrust coefficient = $2(\rho_j V_j/\rho_\infty U_\infty)(V_j/U_\infty - 1)$ (Section 7.3)
C_T	thrust coefficient $=T/(\rho n^2 D^4)$ (Section 7.4)
D	propeller diameter
H	working section height
J	propeller advance ratio, V/nD
n	propeller rotational speed, revolutions per second.
Q_{prop}, Q_{model}	in-tunnel dynamic pressure at propeller plane and model reference point. (Figure 7.23)
Q_S	magnitude of solid blockage source or sink
Q_W	wake blockage source strength
R	propeller radius
T	propeller thrust
T_C	propeller thrust coefficient, $T/(\rho V^2 D^2)$
U	stream speed
V_j	mean jet velocity (Section 7.3)
x	axial distance downstream of the calculated position of the origin of the potential core of the jet. (Section 7.3)
α	(Alpha) model angle of attack
ε	blockage factor (generic $\Delta u/U_\infty$)
ρ	air density
Ω	propeller rotational speed, radians/sec

Suffixes

j	jet or efflux
0, ∞	conditions far upstream of model

7.1 INTRODUCTION

When considering wind tunnel corrections for powered models, a distinction should be drawn between configurations that rely mainly on direct lift or directed thrust and those that obtain most of their lift aerodynamically. We shall see in Chapter 8 that powered flows dominate the interference for VTOL and some STOL configurations and tunnel effects can be large. However, we shall deal in this chapter with cases for which the thrust vector is horizontal or nearly horizontal, including cruise configurations. Airframe aerodynamics and the thrust-drag balance considerations predominate so the effects of the tunnel on airframe aerodynamics are just as important as the effects on the power unit or units.

Wind tunnel corrections can be applied with some confidence to an isolated power unit under calibration or to an unpowered model test, but significant tunnel/flight matching problems can arise when the two are combined. The principle difficulty occurs when a propeller or simulated jet engine is situated some distance away from the model reference point and axial gradient effects are significant. The problem becomes particularly acute for propeller powered models, because of the need to set rotational speed appropriately. However, a similar problem also arises in setting the thrust coefficient for jet-powered models. The subject of power unit settings will be discussed in Section 7.2.

Features peculiar to jet powered models include inlet effects, mass injection effects, vortical structures in powered streams and entrainment effects for high-energy jets. The tunnel interference implications of these effects will be reviewed in Section 7.3.

The special needs of propeller-powered model testing are described in Section 7.4. Classical corrections are described in Section 7.4.1. The remainder of Section 7.4 concerns tests on a generic, propeller-powered model. Section 7.4.2 describes the propeller calibration process and the application of wall pressure signature corrections procedures to it. The problem of separating propeller from model forces in the presence of a tunnel-induced gradient is described in Section 7.4.3. Having extracted the in-tunnel forces and moments on the propeller, the corrections to the residual airframe measurements are described in Section 7.4.4.

7.2 DETERMINATION OF MODEL POWER SETTINGS.

Whether propeller or jet, power units are often located some distance forward or aft of the aircraft c.g. and differences between tunnel interference at the engine location and that at the model reference point become significant. Vertical or lateral interference gradients may also have to be considered.

As an example, consider a conventional single-engine, propeller-driven aircraft model under test in a closed-test section wind tunnel. Depending on the net axial force on the model, blockage may cause either a velocity increase or a decrease along the tunnel axis. A positive axial velocity gradient induced by the tunnel walls will cause the velocity at the plane of a forward-mounted propeller to be less than that at the model reference point. The advance ratio will be lower than in free air and the thrust will be higher. A possible real-time adjustment would be to reduce the propeller RPM as needed to achieve the desired advance ratio. The swirl angles and flow geometry would then be correct, as would the local interactions with the airframe. However, the thrust and the local surface scrubbing would be too low, because of the reduction in velocity over the propeller blades. Another approach would be to retain the original RPM and reduce the blade angle as needed to achieve the required thrust level. The mean blade angle-of attack and CL would then be consistent with the in-tunnel conditions at the model reference point, though the

twist distribution and swirl would be compromised slightly. Rae and Pope [12] discuss the use of thrust and torque balances to select the best blade setting and give a number of other compromises that can be considered. An example of one of the simpler correction procedures will be given in Sections 7.4.3 and 7.4.4.

Except for the rotational aspects, the situation is similar for jet-powered models. Tunnel effects on thrust-drag matching are again an issue, particularly for aft-mounted engines. There is also the question of corrections for mass flow addition when external air is supplied for direct thrust or when using ejector or air-turbine powered engine simulators (see Section 7.3.1). Because of the higher jet speeds, entrainment into the jet, drawing from a finite tunnel mass flow, is a further consideration (see Section 7.3.2).

7.3 Wall Corrections for Jet-Powered Models

7.3.1 The Test Environment

Powered wind-tunnel models suitable for conventional take off and landing aircraft can be divided into two groups:

1. Models representing isolated powerplants, intakes or exhausts to assess the effects of forward speed and angle of incidence or yaw on the characteristics of the powerplant or the component parts of the powerplant.

2. Complete models including simulation of powerplants to assess installation effects.

In both cases the model may inject air into or remove air from the working section. In addition, the effects on wall interference of an exhaust of higher total energy than that of the main flow has to be represented or acknowledged in the method. These flows may be distinguished from the flows over Vertical or Short Take Off and Landing (V/STOL) models considered in Chapter 8 in that the velocity perturbations at the walls are small compared with free-stream speed.

It may be considered that the advent of methods of determining wall interference using measured wall velocities or pressures makes the problem of representing power effects academic. However, when applying these methods, a number of points need to be borne in mind, first, for model-representation methods.

1. A high energy exhaust entrains air from the main flow. Thus to represent a powered model for the calculation of wall interference, a distribution of sinks is required along the axis of the exhaust, as shown schematically in Figure 7.1, together with a source of appropriate strength far downstream to ensure that the static pressure far upstream is not affected by the presence of the model. This effect is likely to be the most serious for high jet velocity ratios, as are found for tests with jet-powered models at low speed, high thrust conditions. The strength of these sinks can be inferred from measurements of static pressure at a number of positions along the walls downstream of the model for solid-wall wind tunnels. For example, provided that the perturbations associated with the model at the wall are 'small', an average of pressures measured at the same streamwise position along the streamwise lines at A and B or C and D could be used in a method such as developed by Hackett et al [6] to determine sink strength for a model at zero lift on the tunnel axis (see Figure 7.1, which illustrates the more general lifting case). For other types of wind-tunnel wall, singularity strength cannot be inferred directly from wall-pressure measurement. Therefore, in this case,

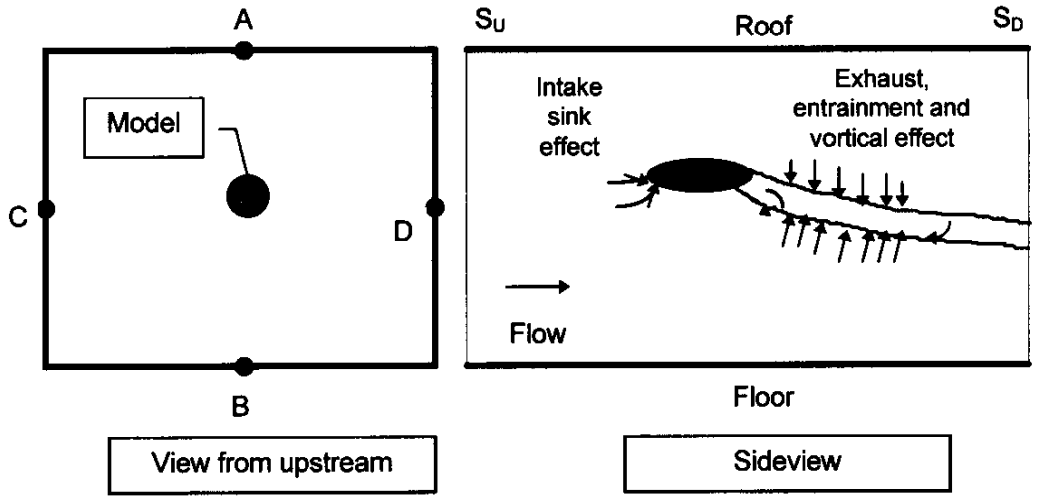

Fig 7.1 A jet-powered, lifting model in a wind tunnel

careful thought needs to be given to the model representation because there could be large errors resulting from the failure to model the direct effect of the model at the walls. This could, in turn, have serious consequences for the estimation of the interference velocity potential at the walls and consequently in the working section.

2. As shown in Figure 7.1, the flow into the intake of a ducted fan or jet engine needs to be represented by either a point sink or a distribution of point sinks on the engine face, the strength of which can be readily estimated knowing the mass-flow characteristics of the powerplant simulator or, if not, by wall pressure measurements made just upstream and downstream of the intake.

3. When the jet axis is inclined relative to the working-section axis, the exhaust is deflected and allowance needs to be made for the antisymmetric effect of the jet. This may be achieved by the use of horseshoe vortices or vortex doublets with axes parallel to the local jet direction. For a solid wall wind tunnel and provided the velocity perturbations at the walls are small compared with the free-stream velocity, the strength of these vortices can be inferred from the difference between the wall static pressures at A and B and for a yawed model from the difference in pressures between C and D (Figure 1).

For two-variable methods the problem of model and jet representation does not arise. However, consideration needs to be given to the conditions at the part of the surface bounding the model far downstream, S_D, as defined in chapter 4.1 and illustrated in Figure 7.1. For a model with a high-energy exhaust, wall pressures can continue to rise some considerable distance downstream of the model. Thus it may not be adequate to use the most downstream pressure measurement as the far-downstream value. A simple expression for the wall pressure coefficient far downstream for powered models has been derived by Ashill and Keating [2].

7.3.2 ENTRAINMENT EFFECTS FOR JET-POWERED MODELS

To illustrate the effects of the intake sink and jet entrainment, results are presented here of wall-pressure measurements made with a jet-powered model in the 13ft x 9ft Low Speed Wind Tunnel at DERA Bedford. This wind tunnel has solid walls. The model comprised an injector-powered nacelle which could either be tested in isolation (Figure 7.2) or in combination with a half model of a wing-body configuration (Figures 7.3 and 7.4). The wing was unswept and cylindrical with a leading-edge slat and a trailing-edge flap. The nacelle could be mounted either 'under' or 'over' the wing as shown in Figures 7.3 and 7.4.

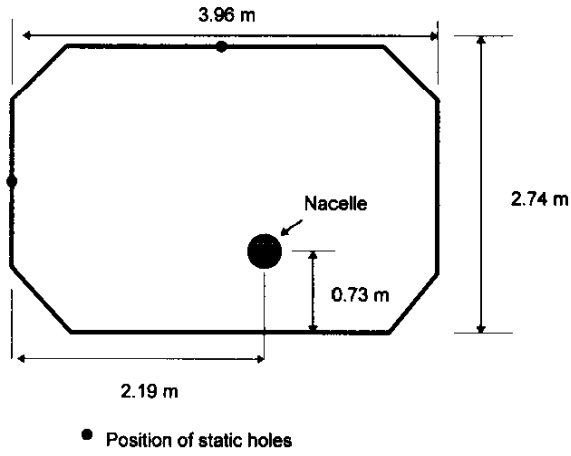

Figure 7.2 View of working section looking downstream, illustrating position of isolated nacelle

Incremental pressures at the roof station due to the effect of power for the isolated nacelle are shown in Figure 7.5. Here the axial distance x is measured downstream of a point about one fan nozzle diameter upstream of the 'hot-jet' nozzle, which corresponds to the calculated position of the origin of the potential core of the jet. The angle of incidence or inclination of the nacelle, α, was obtained by rotating the nacelle about a vertical axis. This axis was offset from the nacelle axis and this explains why the axial positions of the measurement points differ between the three nacelle inclinations. The thrust of the jet is defined by the net-thrust coefficient, C_T, based on the overall area of the nozzle, Aj = 0.02559 m^2 . Thus, since the cross sectional area of the wind tunnel is 10.33 m^2, this implies that Aj/C = 0.00248.

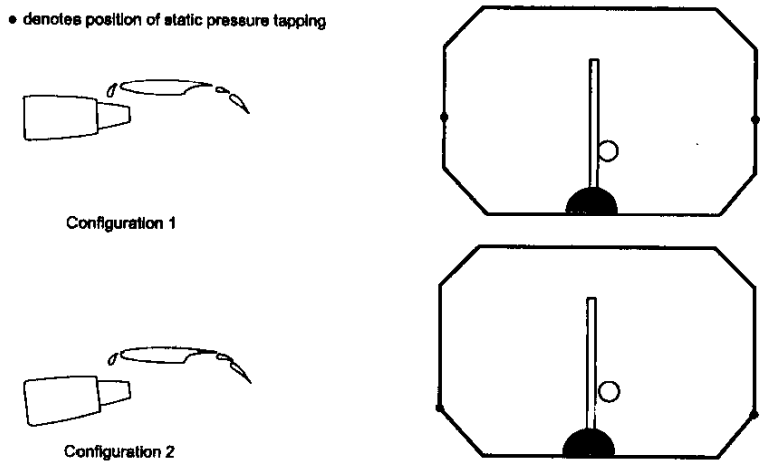

Figure 7.3 Geometry and layout of under-wing nacelle configurations in test section

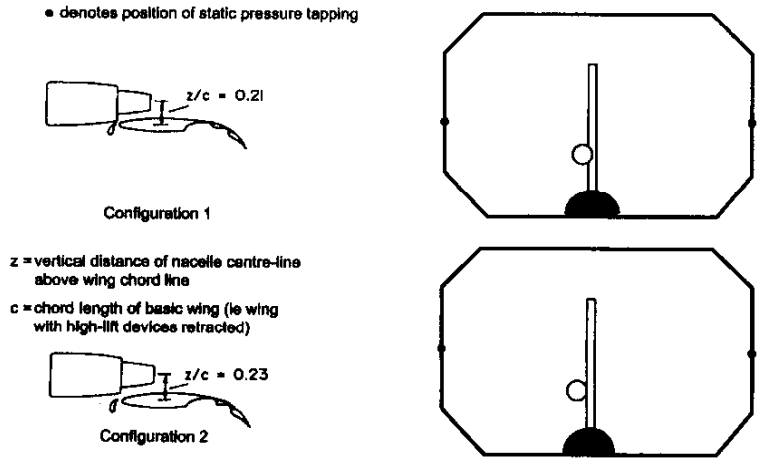

Figure 7.4 Geometry and layout of over-wing nacelle configurations in test section

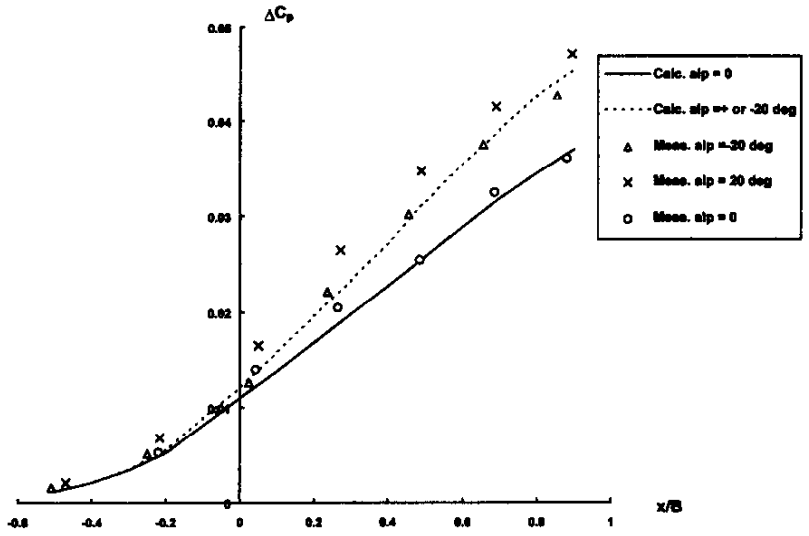

Figure 7.5 Distributions along tunnel axis of incremental pressure coefficient due to thrust at roof station for various nacelle inclinations, isolated nacelle (Fig 7.2), $C_T \approx 33$.

Figure 7.5 shows that the pressure increment increases with axial distance, consistent with the existence of the sink effect of the intake and the jet entrainment. Also shown on the figure are results of calculations made using a model representation method. In this method the intake effect is represented by a sink and the entrainment effect is simulated by an axial distribution of sinks along the jet efflux. The strength of the singularities simulating jet entrainment was determined using the model for jet flows proposed by Bradbury [3] with an empirical modification to allow for jet inclination proposed by Küchemann and Weber [10]. Wall interference was determined by using the method of images. The agreement between calculation and measurement is fairly good, indicating that the main physical features are represented. This suggests that the wall-induced velocities predicted by this method are reliable. Calculations of the wall-induced blockage have been made for similar flows using a two-variable method (Ashill and Keating [2]) and the results of these are also in good agreement with those of the model representation method.

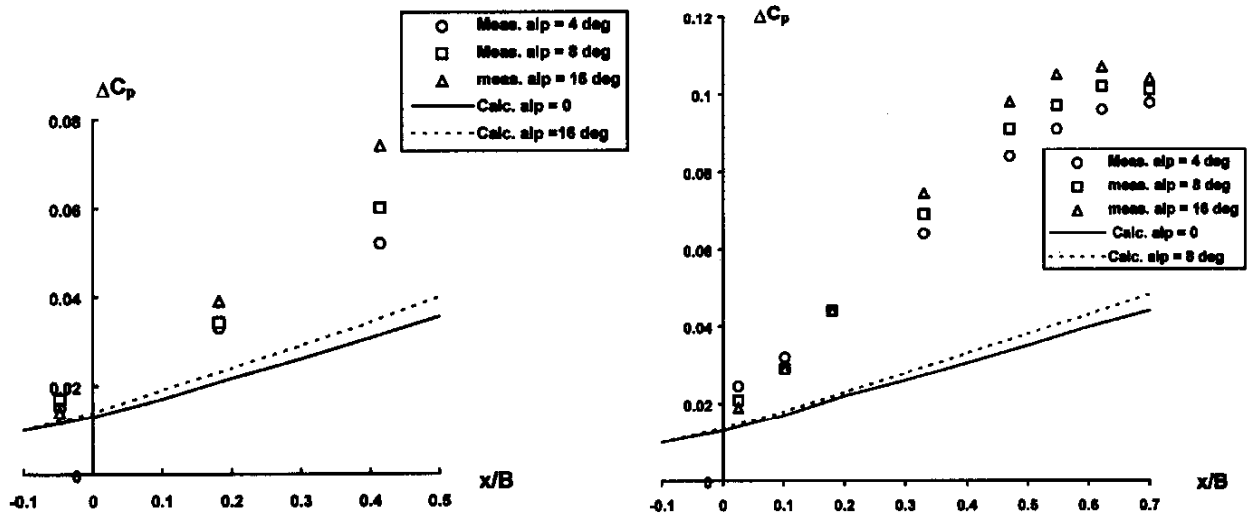

Figure 7.6 Distributions along tunnel axis of mean incremental pressure coefficient due to thrust, under wing configuration Figure 7.3, $C_T = 47.5$

It may be expected that model representation methods are less reliable for more complex flows. Examples of such flows are given in Figure 7.6. The cases shown are for the nacelle mounted under the wing (Figure 7.3), and in these flows the efflux impinges on the lower surface of the flap, providing some lift augmentation by the jet flap effect. To isolate the blockage effect from the lifting (antisymmetric) effect, results are shown for $\Delta\overline{C}_P$ the arithmetic mean of pressure-coefficient increments due to thrust

on opposite walls (see Figure 7.3). In contrast to the isolated nacelle, the model representation method does not give an accurate prediction of the axial variation of the wall pressure increment. However, this method does not allow for the expected large increase in entrainment following the impingement of the efflux on the flap lower surface, with the consequent rapid lateral spreading of the jet. For complex flows of this type wall-pressure signature or two-variable methods are probably the only satisfactory methods available to determine wall interference.

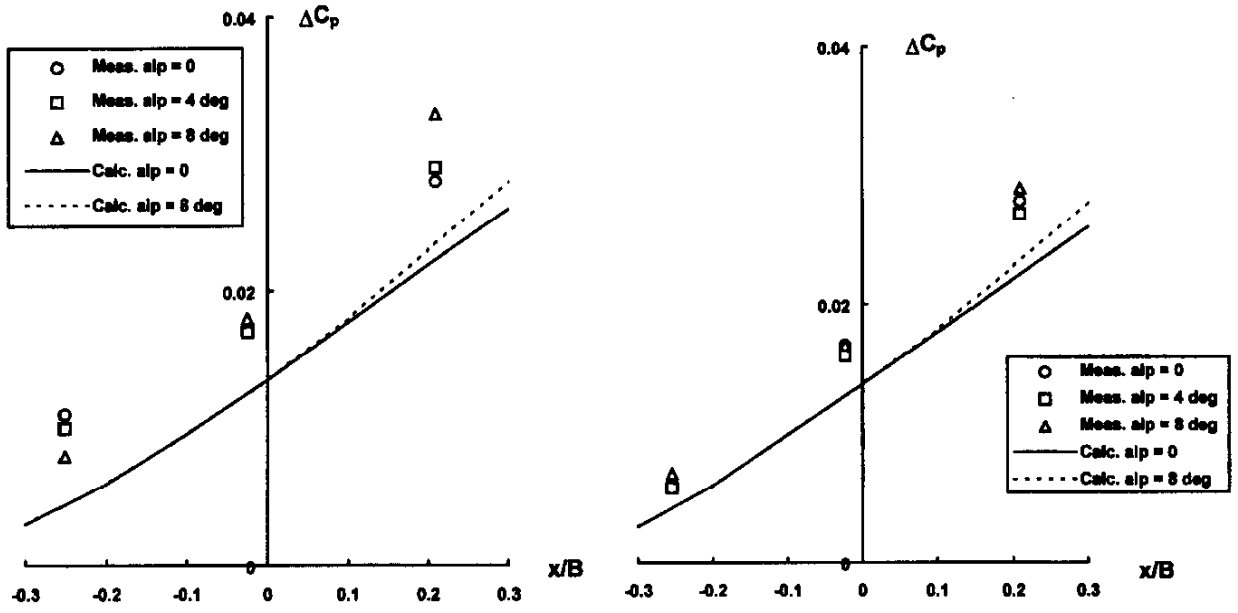

Figure 7.7 Distributions along tunnel axis of mean incremental pressure coefficient due to thrust, over-wing configuration, Figure 7.4, C_T = 47,5

Results for the mean pressure coefficient for a flow of somewhat less complexity is shown in Figure 7.7. In these cases the nacelle is 'over' the wing. Consequently, the efflux does not impinge on the flap. Therefore, there is probably little lateral spreading of the efflux and not much increase in the entrainment effect compared with that for the isolated nacelle. This is reflected in the comparatively good agreement between prediction and measurement in relation to the cases with the nacelle mounted under the wing. However, the agreement between prediction and measurement is not as good as for the isolated nacelle. In summary, these results show the importance of the entrainment effect and indicate the need for wall-signature methods to model the sink effect associated with entrainment.

7.4 WALL CORRECTIONS FOR PROPELLER-POWERED MODELS.

7.4.1 CONVENTIONAL CORRECTION METHODS

ADDITIONAL SYMBOLS for Section 7.4.1

A	streamtube cross-sectional area
C_T	thrust coefficient, Eq.(7.21)
f	auxiliary quantity, Eq.(7.5)
m	sink strength
r	distance from propeller centre
V	axial velocity
X	auxiliary quantity, Eq.(7.6)
α	blockage ratio, Eq.(7.2)
ε_T	thrust blockage factor
Φ	perturbation potential
η	ideal efficiency, Eq.(7.17)
λ	uncorrected to corrected stream velocity, Eq.(7.1)
σ	propeller disk area to slipstream cross-section far downstream, Eq.(7.4)
τ	Glauert's thrust coefficient, Eq.(7.3)

Suffixes

c	corrected
p	propeller (actuator disc)
T	associated with thrust
0	far upstream
1	far downstream

7.4.1.1 GLAUERT'S METHOD

Using the axial momentum theory, the problem of wall interference on a powered propeller tested in a solid-wall wind tunnel at low subsonic speeds has been solved in the 1930's by Glauert and is described in detail in his monograph (Glauert [5]). The corrected wind-tunnel stream velocity is defined as the free-stream velocity which for a given value of thrust provides the same axial velocity at the propeller as that observed in a wind tunnel. Combined with the appropriate laws of conservation, this condition determines the ratio of the uncorrected and corrected stream velocities,

$$\lambda = \frac{V}{V_c} \tag{7.1}$$

as a function of the blockage ratio

$$\alpha = \frac{A_p}{C} \tag{7.2}$$

and thrust coefficient

$$\tau = \frac{T}{\rho A_p V^2} \tag{7.3}$$

The pertinent geometrical parameters of a slipstream (propulsive streamtube) inside a wind tunnel are shown in Figure 7.8 a. Introducing

$$\sigma = \frac{A_1}{A_p} \tag{7.4}$$

the interdependence is described by the system of 4 non-linear equations

$$f = \frac{(1-\sigma)(1-\alpha\sigma)}{\sigma\left(1-\alpha\sigma^2\right)^2} \tag{7.5}$$

$$x = \frac{1+f}{1-f} \tag{7.6}$$

$$\lambda = 1 + (x-1)\alpha\sigma^2 - \frac{(2\sigma-1)x-1}{2\sigma} \tag{7.7}$$

$$\tau = \frac{(x+1)(x-1)}{2\lambda^2} \tag{7.8}$$

in 4 unknowns: σ, f, x, and λ .

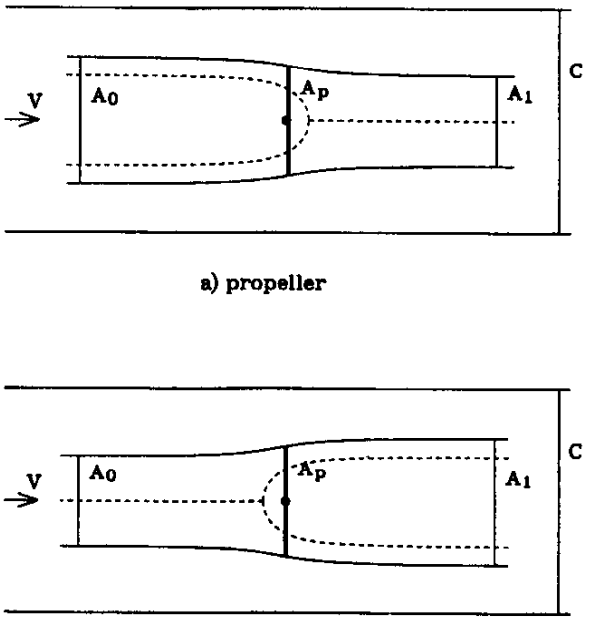

Figure 7.8 Cross-sections of a slipstream and wind tunnel

To evaluate λ for the given α and τ , Glauert makes successive sweeps through Eqns. (7.5-7.8), adjusting σ until the prescribed value of τ is obtained. For a small blockage ratio α a suitable initial guess is the value of σ in free air :

$$\sigma = \frac{1+\sqrt{1+2\tau}}{2\sqrt{1+2\tau}} \tag{7.9}$$

as may be derived from the subsequently introduced Eqns.(7.10), (7.11) and (7.15).

Although Glauert's method does not result in a simple correction formula, the procedure can easily be coded for a personal computer, producing corrections in a matter of seconds. The Appendix to this section contains the listing of a C-language code which updates σ by targeting on τ by the method of secants. The results, which were found to satisfactorily duplicate the original correction data produced by Glauert [5], are plotted by solid lines in Figure 7.9.

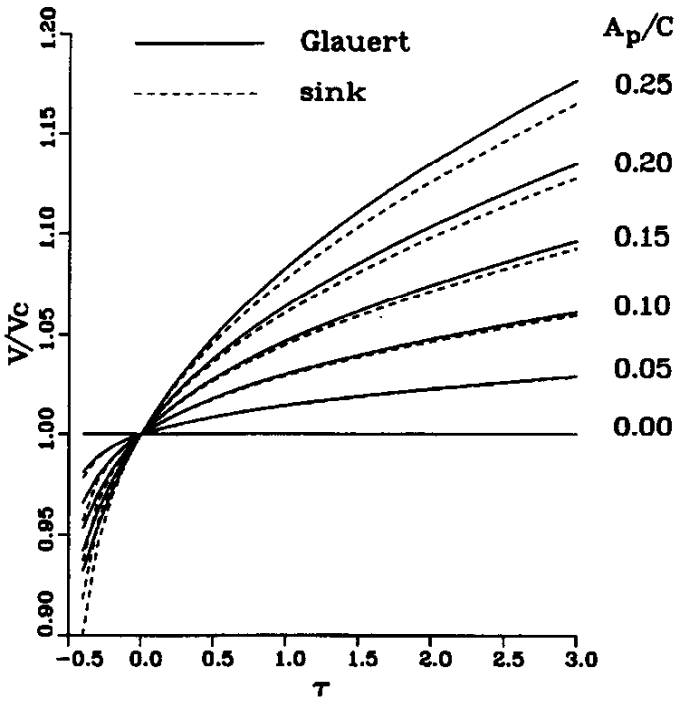

Figure 7.9 Ratio of uncorrected and corrected stream velocities in a solid wall wind tunnel

Glauert's method has successfully stood the test of time and became a standard method for correcting low-speed propeller tests in solid-wall wind tunnels (AGARD [1]) The limitations of the method are that it does not account for the actual shape of the test section and that axial momentum analysis is impossible to extend to ventilated-wall test sections if flow through the walls is not exactly known. Since until recently no alternative method of correction in ventilated wind tunnels has been devised, a large number of propeller tests in the past have been intentionally conducted in solid-wall test sections.

7.4.1.2 REPRESENTATION OF A PROPELLER BY A SINK. [1]

As already discussed in chapter 7.4.1.1, the contraction or expansion of the wakes of propellers or windmills can be represented by sinks or sources respectively. This approach opens the doors to the conventional techniques of accounting for wall interference (images, one-variable method, etc.), which are also applicable to test sections of arbitrary geometry or ventilation.

Conservation of mass for incompressible flow inside the propeller streamtube, Figure 7.8a, implies

$$A_0 V_0 = A_p V_p = A_1 V_1 \tag{7.10}$$

From the Rankine-Froude theory it further follows that the axial velocity at the propeller is the average of the upstream and downstream axial velocities

$$V_p = \frac{1}{2}\left(V_0 + V_1\right) \tag{7.11}$$

The perturbation observed in the far field (near the walls) can be represented by the potential of a sink

$$\varphi = \frac{m}{4\pi r} \tag{7.12}$$

where r is the distance from the propeller centre. The strength m, given by the contraction of the slipstream, is from Eqns.(7.10) and (7.11)

[1]Note that, in this section, source strength has units of length-squared.

$$m = A_0 - A_1 = A_p\left(\frac{V_p}{V_0} - \frac{V_p}{V_1}\right) = \frac{1}{2}A_p\left(\frac{V_1}{V_0} - \frac{V_0}{V_1}\right) \tag{7.13}$$

Equation (7.13) can be derived more rigorously using the Stokes' stream function for a sink in uniform stream (Mokry [11]). It can also be shown that if the slipstream boundary is represented by a stream surface passing through the propeller disk circumference, the location of the sink is slightly upstream of the propeller disk. However, for typical test conditions this distance is negligible compared to the dimensions of the working section.

By the Rankine-Froude theory the thrust is given by

$$T = \frac{1}{2}\rho\left(V_1^2 - V_0^2\right)A_p \tag{7.14}$$

and, using Eqn.(7.3) thus

$$\frac{V_1}{V_0} = \sqrt{1+\frac{V_1^2 - V_0^2}{V_0^2}} = \sqrt{1+\frac{2T}{\rho A_p V_0^2}} = \sqrt{1+2\tau} \tag{7.15}$$

Substituting in Eqn.(7.13) it follows (Mokry [11])

$$m = \frac{1}{2}A_p\left(\sqrt{1+2\tau} - \frac{1}{\sqrt{1+2\tau}}\right) \tag{7.16}$$

The sink strength can also be related to the efficiency of the propeller. The ideal (Froude) efficiency is

$$\eta = \frac{2V_0}{V_0 + V_1} = \frac{2}{1+\sqrt{1+2\tau}} \tag{7.17}$$

Evidently, $\eta \to 1$ as $V_1 \to V_0$ or $\tau \to 0$, in which case $m \to 0$. Conversely, $\eta \to 0$ as $V_1 \to \infty$ or $\tau \to \infty$, whereby $m \to \infty$. From these limits it is apparent that for a given propeller disk area, A_p the sink representing a more efficient propeller is smaller than that representing a less efficient propeller. This is of no surprise, since the efficiency of propulsion, defined as the ratio of the useful work to the total work, is higher if the propeller produces less thrust per unit propeller area.

We shall now discuss how the sink approach compares with Glauert's correction method. Towards this end, consider an infinitely long wind tunnel having a circular cross-section of area C and place a sink of strength m on its axis. Interpreting the corresponding wall interference effect as a negative wake blockage, the correction to the stream velocity at the sink is (Wright [14])

$$\Delta V = -\frac{Vm}{2C} \tag{7.18}$$

The ratio of uncorrected and corrected velocities is thus

$$\frac{V}{V_c} = \frac{V}{V + \Delta V} = \left(1 - \frac{m}{2C}\right)^{-1} \tag{7.19}$$

The sink strength is calculated from Eqn.(7.16) and the evaluated velocity ratio compared with that obtained by Glauert's method, chapter 7.4.1. The results shown in Figure 7.9 indicate that for blockage ratios Ap/C < 0.10 there is a close agreement of both methods. The discrepancy at larger blockage ratios is due to the fact that Glauert's correction technique utilises conservation of the axial momentum. To enforce agreement with Glauert, the sink strength would have to be adjusted (increased) as the blockage

ratio grows. This confirms some more recent observations (Hackett [7]) that singularities representing a model in the wind tunnel should be considered wind-tunnel dependent. For propeller-wing-body combinations, it is more convenient to work with the thrust blockage factor, which for a solid-wall test section is given by

$$\varepsilon_T = \frac{V_c}{V} - 1 = \frac{\Delta V}{V} = -\frac{m}{2C} \tag{7.20}$$

The thrust blockage factor is additive with the solid and wake blockage factors representing the other components of the model and their wakes. Substituting for m from Eqn.(7.16) and introducing an alternative form of the thrust coefficient

$$C_T = 2\tau \tag{7.21}$$

we obtain the thrust blockage factor for a solid-wall test section (Kupper [9]) :

$$\varepsilon_T = -\frac{A_p}{4C}\frac{C_T}{\sqrt{1+C_T}} \tag{7.22}$$

Although the sink method is less rigorous than that by Glauert, its advantage lies in the fact that it is also applicable to working sections having ventilated walls. The extension of Eqn.(7.18) to ideal porous-slotted wall is obtained by using the theoretical result derived for a source by Wright [14]. The discussion of methods appropriate to ventilated working sections in general is given in Sections 3 and 4.3.

The evaluation of the sink strength for a compressible-flow slipstream is considerably more involved, since the axial velocity is discontinuous across the propeller disk and power is not uniquely determined by thrust. However, for highly efficient propellers at Mach numbers up to about 0.8, the value of m obtained from Eqn.(7.16) is adequate for the practical evaluation of blockage (Mokry [11]).

7.4.1.3 CORRECTIONS FOR A WINDMILL IN A WIND TUNNEL.

The axial momentum theory can also be applied to wall interference on a windmill tested in a wind tunnel. Since the windmill is designed to take power from the wind tunnel stream, it will experience a negative thrust or drag. The fluid is decelerated in the streamwise direction as the cross section of the slipstream increases, see Figure 7.8 b. Assuming $0 < V_1/V_0 < 1$, it follows from Eqn. (7.15) that for a windmill the thrust coefficient is restricted to the interval $-0.5 < \tau < 0$. To our knowledge, Glauert [5] has not considered applying his method to the windmill problem, but as the reader may have already noticed in Figure 7.9, the method produces results even for the negative values of thrust. The only difficulty is experienced when approaching the lower limit $\tau = -0.5$, where the slopes of the V / V_C vs τ curves become very large and the method of successive approximations fails.

The far field effect of the windmill can also be represented by Eqns.(7.12-7.13). Since $A_1 > A_0$, we obtain $m < 0$, indicating that the singularity described by Eqn.(7.12) is a source. A practical evaluation of the velocity correction can be done as for the wake blockage, see for example Section 2.2.2.3. Another reference is made to windmill testing in chapter 7.4.2.1 .

7.4.2 PRESSURE SIGNATURE-BASED CORRECTION METHODS: PROPELLER CALIBRATION

This sub-section and the next will describe the application of the wall pressure signature method to a generic single-engined trainer model with a tractor propeller. The propeller was small compared to the

tunnel cross section, having a disk area only 2.02% of the test section area. Nonetheless, the data obtained were of good quality and the limited model size did not impede the present demonstration of correction methods. We shall consider first the application of the method to the propeller calibration process. Application in a whole-model test will be described in sections 7.4.3 and 7.4.4.

7.4.2.1 PROPELLER CALIBRATION: DIRECT TUNNEL EFFECTS.

The propeller was mounted on the tunnel centreline at the front of a long body that could be yawed. Pitch capability was unnecessary because the rig was axisymmetric. The propeller and drive motor were metric and forces and moments on them were transmitted to a below-floor tunnel balance. The cylindrical shielding around the motor and drive was non-metric and pressure taps were provided behind the spinner and at other locations on the metric/non metric interface. These were used to estimate pressure tares. Body tares and baseline roof pressures were measured with the propeller removed.

Figure 7.10(a) shows pressures measured on the wind tunnel roof during propeller calibration. Baseline pressures have been removed and the reference levels reset from an upstream to a downstream datum. Increasing pressures and decreasing velocities (Figure 7.10(b)) may be seen as the slipstream contracts. The lowest T_C value (filled circles) had no power input to the motor and the windmilling propeller produced a small drag.

The source-source-sink version of the pressure signature program is appropriate for analysing data of the present type. However, the standard program does not work properly for the propeller tested alone, because of the absence of a solid blockage 'hump' in the pressure signature (see Figure 7.10(a)). As an

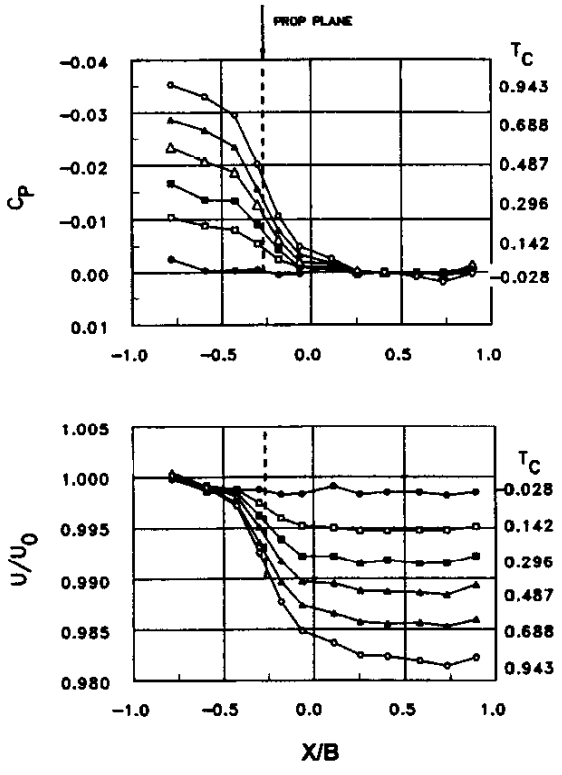

Figure 7.10 Typical data from propeller calibration test
(a) Measured tunnel roof cps
(b) Derived surface velocities

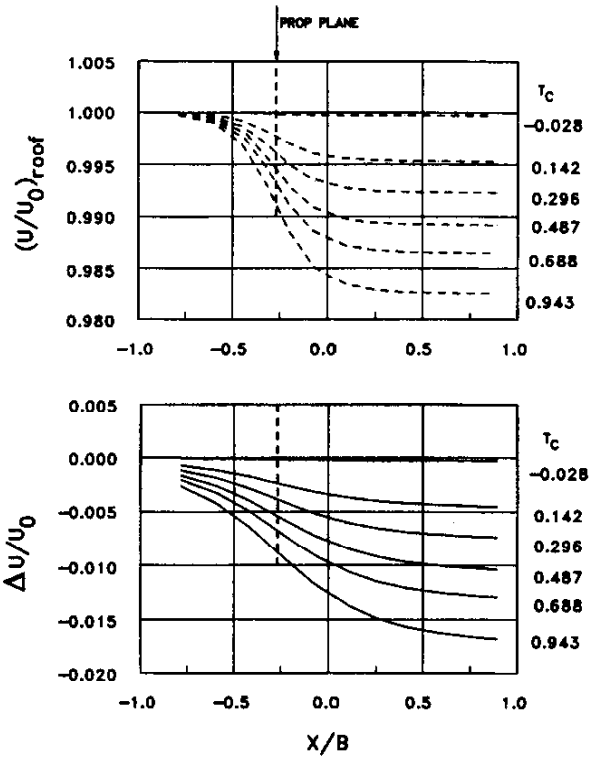

Figure 7.11 Tunnel conditions derived from wall pressures
(a) Velocities at the tunnel roof
(b) Centreline interference velocities

alternative, it was found that a single sink placed at the centre of the propeller represents it very well for estimating blockage. Figure 7.11(a) shows calculated roof velocities based on a single sink, and its wind tunnel images, whose strength was chosen by matching the measured asymptotes of Figure 7.10(b). Overlaying these two figures showed that the single sink represents the propeller well. Differencing the two data sets revealed only small random variations, with no discernible trends. Figure 7.11(b) shows the corresponding centreline interference that represents a decrease in velocity from the set value.

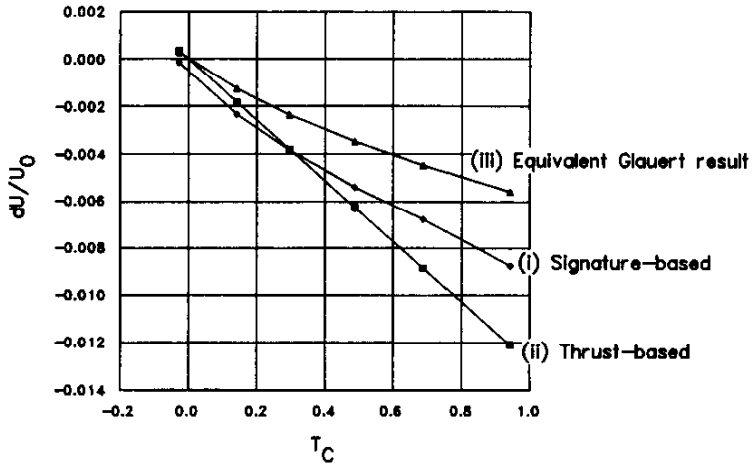

Figure 7.12 Changes in tunnel speed due to image effects

The interference velocities at the propeller plane, shown in curves (i) and (ii) of Figure 7.12, are used to estimate both the q-correction at the propeller and the change in thrust that occurs due to the change in advance ratio. Curve (i), which is a cross-plot of Figure 7.11(b), shows pressure signature results. Curve (ii), based on measured thrust, represents the classical result. The signature-derived interference velocities are about 75% of the force-derived ones. The difference between these curves is attributed to increased scrubbing drag on the centrebody and possible changes in tunnel-wall skin friction caused by propeller-induced pressure gradients. Both increase the positive blockage, compared with the thrust-derived result.

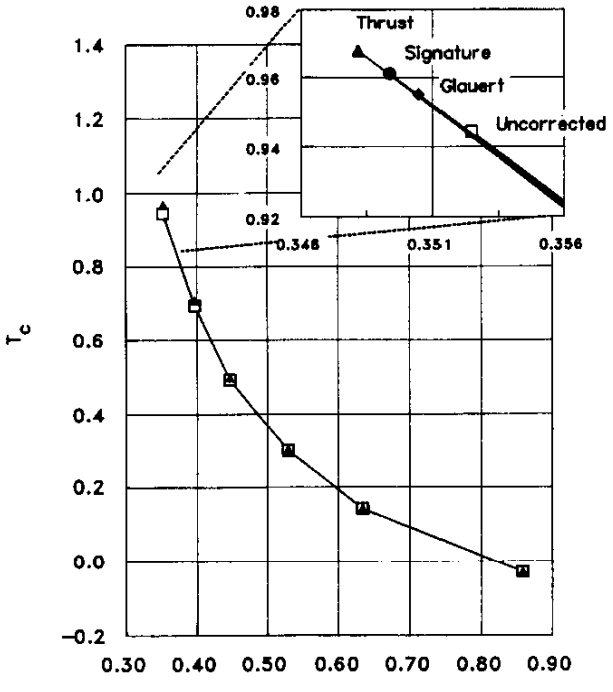

Figure 7.13 Uncorrected and corrected propeller characteristics

Curve (iii) of Figure 7.12 is the Glauert result of the previous section, expressed as an increment. This result is solely thrust-based so it is surprising, at first, that the interference increment is only about half of that of curve (ii), which is also thrust-based. However curves (i) and (ii) reflect only the effects of velocity changes whereas the Glauert analysis gives an equivalent velocity that includes other effects.

Figure 7.13 shows the result of applying the corrections of Figure 7.12 to the propeller characteristic curve. Figure 7.14 gives the same information in a more visible, incremental form. It is emphasised that only corrections to thrust coefficient and advance ratio, as they occur in the tunnel, are involved at this point. Interactive effects, which will be discussed later, affect the measured thrust but are not involved directly in the tunnel corrections.

As already mentioned, the present model and its interference increments are small. The characteristics of the various correction procedures are illustrated by the top point of the propeller characteristic, shown inset in Figure 7.13. As already noted, the blockage is negative for a thrusting propeller. The thrust-based procedure, which parallels one of the standard methods used for drag (the 'quarter S/C' method), gives the greatest correction. Viscous effects in the tunnel test section are the most probable cause of the reduction in signature-based interference compared with the thrust-based value.

Both the Glauert and the pressure signature procedures recognise the higher total pressure of the slipstream. This is explicit for Glauert's analysis but occurs in the pressure signature method because real flow measurements are used. However, the downstream condition employed by Glauert differs from the other two methods when changes at the model are calculated. At this stage, neither the thrust-based and signature methods recognise the dual-stream condition but Glauert's momentum analysis does. It is not clear whether this is the reason for the lower interference given by the Glauert correction.

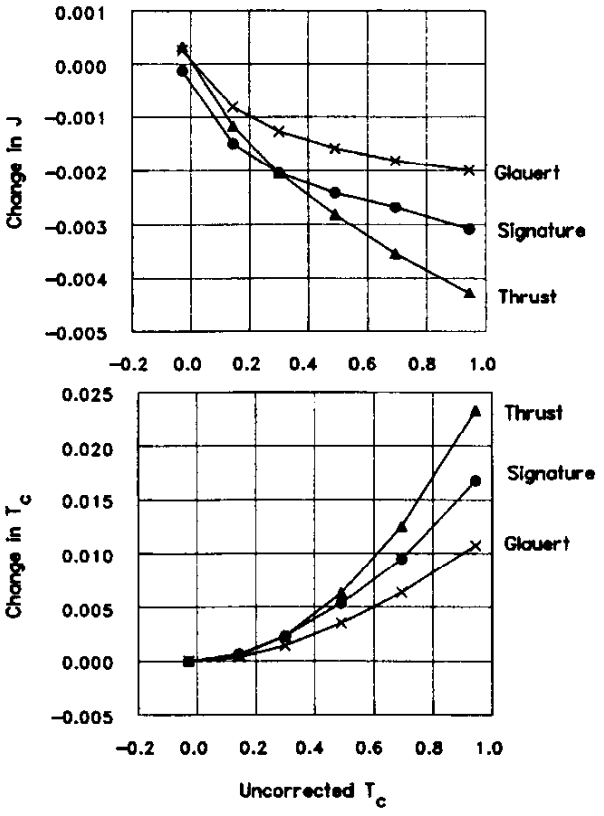

Figure 7.14 Changes in propeller parameters due to blockage (a) advance ration
(b) thrust coefficient

7.4.2.2 AXIAL GRADIENT EFFECTS

Hackett [7] describes the effect of an axial gradient on a separation bubble behind a normal flat plate (see also Chapter 6 of this document). A drag increment is derived, proportional to source-strength squared, that represents an in-tunnel drag increase. Similar principles apply for propeller testing except that the senses of the gradients and the resulting drag increments are reversed. It is suggested that

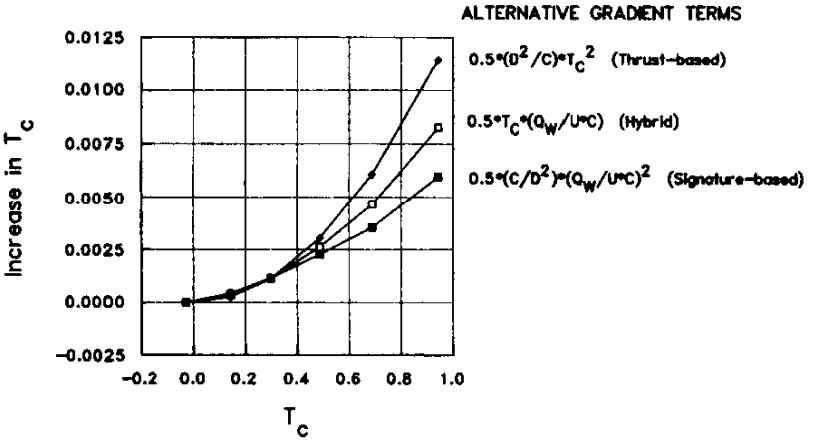

Figure 7.15 Gradient induced thrust increases on a propeller during calibration

adverse pressure gradients (e.g., Figure 7.10(a)) shorten the slipstream contraction and cause an increase in thrust that would not occur in free air. This effect is quite distinct from the effect of changes in velocity itself. The result just discussed is hypothetical because the appropriate experimental verifications have not been done for propellers[2]. Figure 7.15, which shows the gradient corrections for the present model, is therefore presented here for information only.

The gradient corrections shown in Figure 7.15 have the same magnitude as the velocity corrections of Figure 7.14. Three versions of the gradient correction procedure are shown. These parallel those discussed by Cooper et al [4] for drag corrections, but are expressed here in terms of the thrust coefficient, T_C. The upper curve in Figure 7.15 is completely thrust-based and would be the only option if wall pressures were unavailable. The lower curve is totally wall-signature based. The curve marked 'hybrid' includes both and is the result of choice. This curve employs measured thrust to determine the source strength and the pressure signature to find the velocity increment applied to it.

7.4.2.3 INTERACTION WITH TUNNEL-INDUCED VELOCITIES.

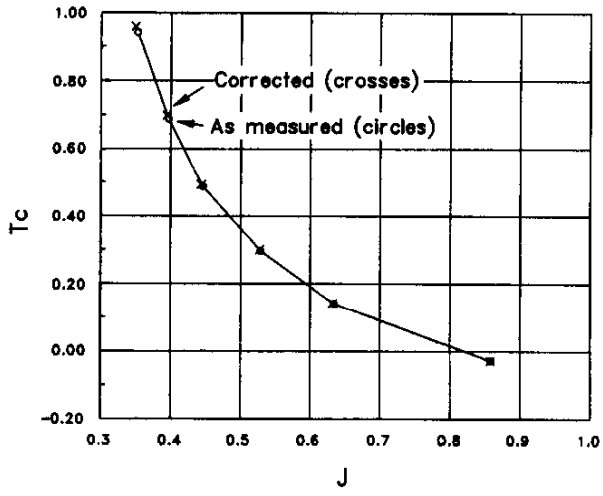

Figure 7.16 Effect of tunnel induced reduction in advance ratio

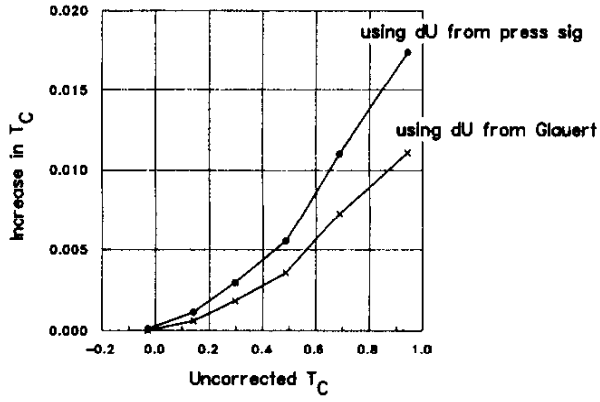

Figure 7.17 Increases in T_C due to tunnel induced reduction in J

The tunnel-induced reduction in velocity at the propeller plane causes the advance ratio to fall below the nominal value at the model reference point (see Figure 7.14(a)). This causes an increase in thrust that would not occur in free air. Figure 7.16 shows this on the propeller characteristic curve. The effect is quite distinct from the tunnel correction procedures just described which, in two of the three cases, involve only velocity renormalisation.

The apparent similarity between Figures 7.13 and 7.16 is deceptive. The shifts in Figure 7.13 are caused by renormalisation on both axes but those in Figure 7.16 reflect thrust increments that are caused by tunnel-induced changes in advance ratio. The advance ratios for the circles in Figure 7.16 are based on the uncorrected tunnel speed. The crosses are placed on the existing curve at the corrected J, using data from Figure 7.14(a). Thrust increments are then read from the curve. The results are summarised in Figure 7.17 for the Glauert and the pressure signature analyses.

Comparing Figure 7.17 with Figure 7.14(b), it is seen that the in-tunnel increase in thrust due to reduced advance ratio and the change due to velocity renormalisation are of similar size. Both the interactive and the direct increments are higher for the pressure signature approach than for the Glauert treatment.

[2] The experimental verification has, however been done for windmills (see He Dexin (1986))

7.4.3 SEPARATION OF PROPELLER AND AIRFRAME FORCES AND MOMENTS.

7.4.3.1 INTRODUCTION

This section concerns the resolution of whole-model forces and moments into airframe and propeller contributions. There are two motivations. From a project point of view, resolved airframe-only data can be combined, without further testing, with propeller data for a different blade angle or blade design. The implicit assumption is that propeller-airframe interactions at a given thrust level are not significantly different from the baseline. From a test point of view, it is essential to remove propeller forces and moments before applying tunnel constraint corrections to the rest of the airframe. This is because of the peculiarities of propellers, particularly their sensitivity to forward speed. The appropriate tunnel corrections are applied separately to prop and airframe data. Corrected forces and moments can then be recombined as needed.

The preferred way of separating propeller and model forces is to use a propeller balance. This gives not only a direct measurement of thrust and other forces but also propeller torque, which is of great interest in its own right. However such balances increase test complexity and cost significantly and a procedure using an extended propeller calibration (see Section 7.4.2) is frequently used instead. A procedure for using such a calibration will be described below.

Either the prop-balance or the calibration approach gives a set of uncorrected airframe forces and moments and a corresponding set of uncorrected propeller forces and moments. With certain exceptions that will be described in Section 7.4.4, conventional tunnel corrections may be applied to the airframe data. Tunnel effects are recognised as a part of the propeller-force removal process, below, but this does not address the conversion of propeller forces to the free air condition. This will be described in Section 7.4.4

The discussions below start with a step-by-step review of the thrust-removal process, followed by a test example that illustrates some major features. The step-by-step procedure covers combined pitch and yaw conditions but the test examples will be for zero-yaw only.

7.4.3.2 STEP-BY-STEP PROCEDURE

If prop-balance data are unavailable, propeller force and moment calibrations (see 7.4.2) may be employed. These calibrations include off-axis angles and are corrected to the free-air condition. The following procedure is used to remove the forces and moments acting directly on the propeller from the measured whole-model values:

(1) Calculate the total in-tunnel velocity and dynamic pressure at the propeller hub. Adjustments for tunnel blockage effects must be included. Tunnel-induced upwash effects may need to be considered but lateral constraint effects are generally found to be insignificant.

(2) Starting with aircraft pitch and yaw angles, determine the total inflow angle between the mainstream velocity vector and the propeller axis and the roll angle around the prop axis at which this occurs. The off-axis angle is equivalent to the yaw angle in the calibration described above.

(3) Calculate the propeller advance ratio using the total velocity found in (1).

(4) Using the propeller calibration at the off-axis angle and advance ratio calculated in (2) and (3), determine the thrust coefficient and the other five force and moment coefficients acting on the propeller. The calibration gives these in the off-axis/roll angle co-ordinates. These forces and moments are normalised using the dynamic pressure at the propeller hub.

(5) Resolve the forces and moments just found to aircraft wind-axis co-ordinates and transfer them to the model reference point. Adjust for any alignment differences and offsets between the propeller and model axes.

(6) Re-normalise the propeller force and moment coefficients found in (5) by multiplying by the ratio of 'q' at the propeller to 'q' at the model reference position or by applying an equivalent incremental correction.

(7) Subtract the propeller force and moment coefficients generated in (6) from the corresponding whole-model values.

The in-tunnel forces and moments on the propeller have now been removed from the measured data leaving the airframe loads, which include slipstream-induced loads. The main tunnel corrections remain to be done.

7.4.3.3 APPLICATION TO A SINGLE-ENGINED TEST MODEL

The single-engined model had a tractor-propeller with a disc area of 2.02% of the tunnel cross section. The wing span was 57.3% of the tunnel width and the wing area was 7.09% of the tunnel cross section. The model was mounted on the centreline of the tunnel. Mid-height sidewall pressures were measured for blockage estimation.

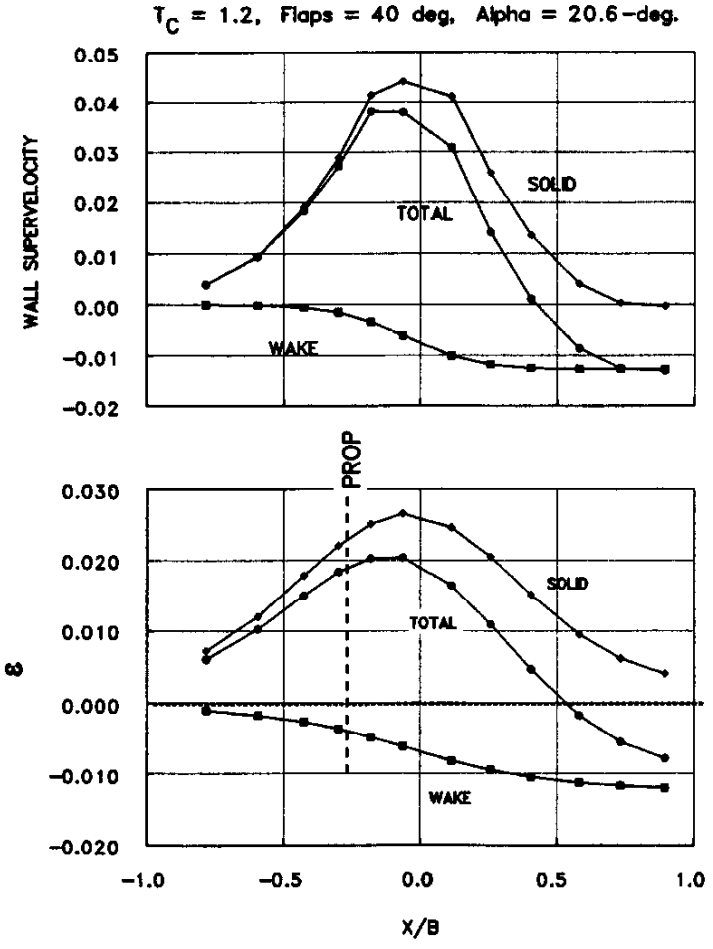

Figure 7.18 Wall signature analysis and resulting interference distribution

Figure 7.18 shows a typical set of sidewall data (upper plot) resolved into solid and wake-related components. At a thrust coefficient, T_C, of 1.2 and 40-deg flap there is excess thrust and a descending profile is seen for the wake component of the signature. The lower plot shows interference velocities derived from the measurements. The most noticeable feature of the total interference curve is the strong negative interference gradient aft of the model. The difference in total ε between the model reference point, at X=0, and the propeller plane is very small for this particular case.

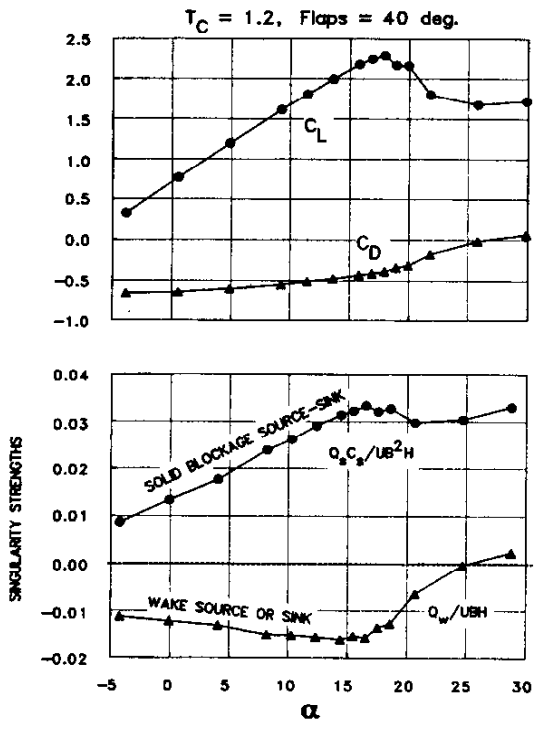

Figure 7.19 Measured force and flow model characteristics

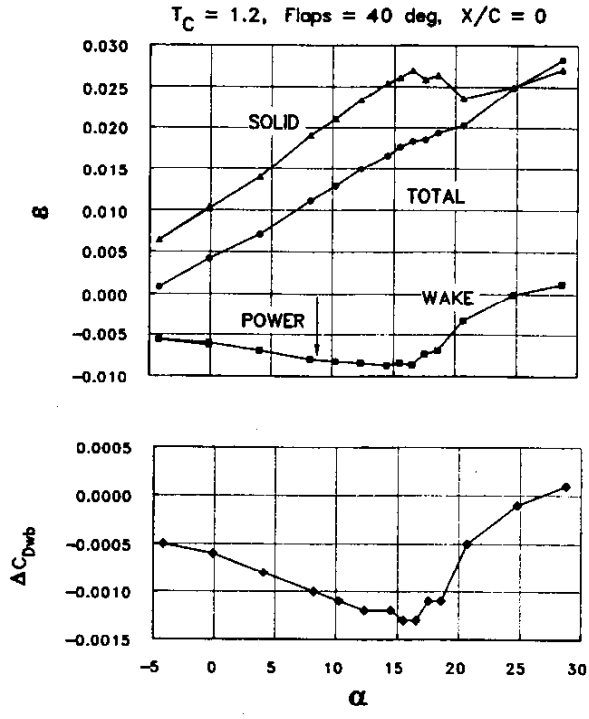

Figure 7.20 Interference break down as a function of angle-of-attack

Figure 7.19 (upper plot) shows the lift and drag characteristics of the model for T_C = 1.2 and 40-deg flap, together with solid and wake singularity strengths (lower plot) derived from pressure signatures. At this thrust level, the propeller thrust dominates the wake source strength until well into the stall. The product Q_SC_S represents the effective doublet strength of the model and follows the same trend as the C_L curve. Figure 7.20 (upper) shows blockage velocities generated using the solid and wake blockage singularities of the previous figure. The total interference increases continuously with angle-of-attack: the post-stall reduction in solid blockage is offset by an increase in wake blockage. The lower plot, which shows the wake-induced blockage increment, follows the trends of the wake source strength itself.

The variation of blockage with power and angle-of-attack may be seen in Figure 7.21. At zero-T_C (upper plot), all the blockage velocities are positive and a rapid increase in blockage at stall is clearly evident. Adding power, with

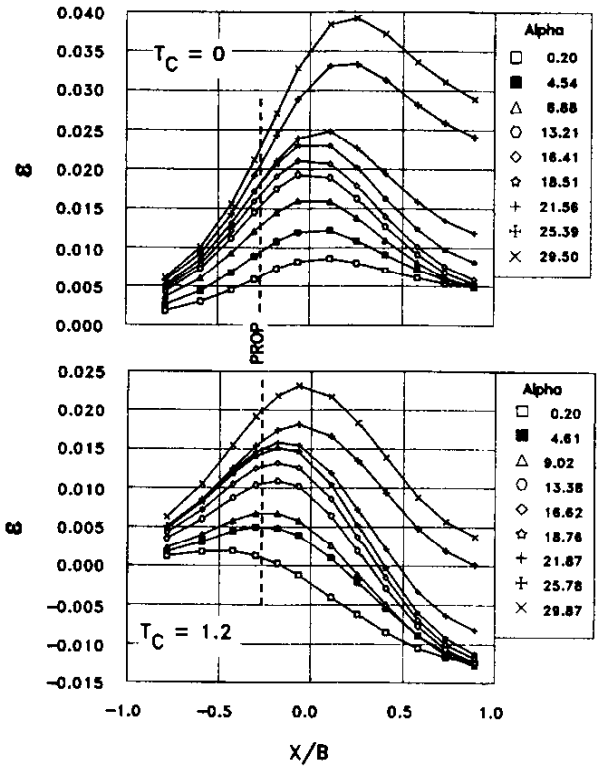

Figure 7.21 Interference at various angles-of-attack, and thrust coefficients of zero and 1.2, (no flap)

zero flap (lower plot), reduces the blockage velocities markedly and increases the negative gradient aft of the model. The increment in between the propeller and model reference locations can be either positive or negative, depending on angle-of-attack. This increment determines the adjustment that must be made to the nominal J-value before reading propeller thrust from the propeller calibration curves in Step (4), above.

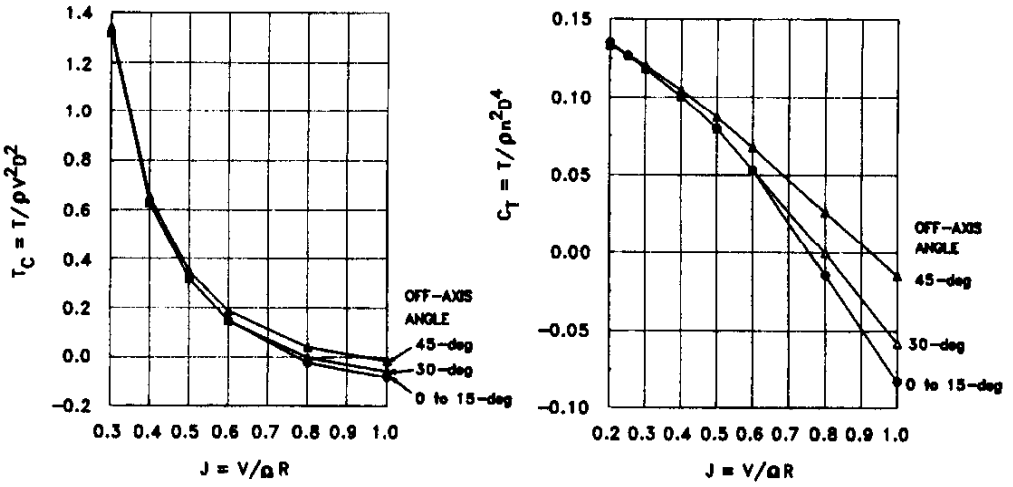

Figure 7.22 Effects of off-axis angle on propeller calibration. a) as T_C, b) as C_T

The propeller characteristics are presented in terms of T_C in the left plot of Figure 7.22. Curves are shown for off-axis angles ranging from zero to 45-degrees. In the examples shown here, which are for zero-yaw, the off-axis angle equals the angle-of-attack[3] and the resolution process is very straightforward. At combined yaw and angle-of-attack, the resultant off-axis angle must be used when accessing the relevant propeller curves.

Expressed in terms of T_C, the off-axis angle effect appears weak. However it becomes more noticeable when the characteristic is expressed as C_T (right plot in Figure 7.22). Advantages of using C_T include the fact that the divisor does not include forward velocity (and so is unchanged by tunnel interference) and the fact that the characteristics are less curved. Either form may be used in Step (4), however. A similar look-up approach is employed for other forces and moments.

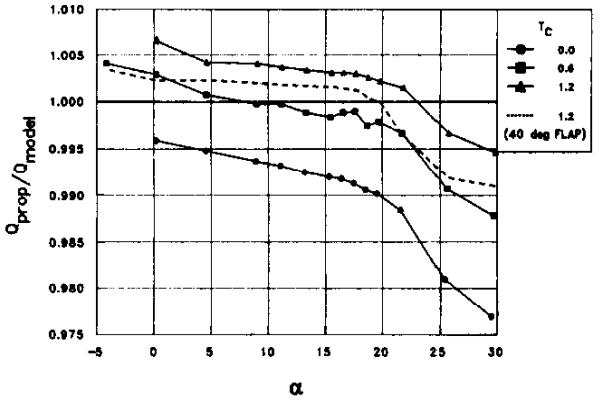

Figure 7.23 Ratio of dynamic pressures for propeller and model positions

Most propeller aerodynamic parameters are normalised on dynamic pressure at the propeller. They must therefore be re-normalised to conditions at X = 0 before subtracting them from whole-model values. Figure 7.23 shows the dynamic pressure ratio, used in Step (6), between propeller and model reference locations. This ratio can be greater or less than unity, depending on thrust, angle-of-attack and flap setting.

[3]Tunnel induced upwash was small and the propeller calibration was not very sensitive to angle so no tunnel correction was made to angle of attack in step 1. Tunnel induced upwash effects may need to be included in this step for larger, multi engined configurations.

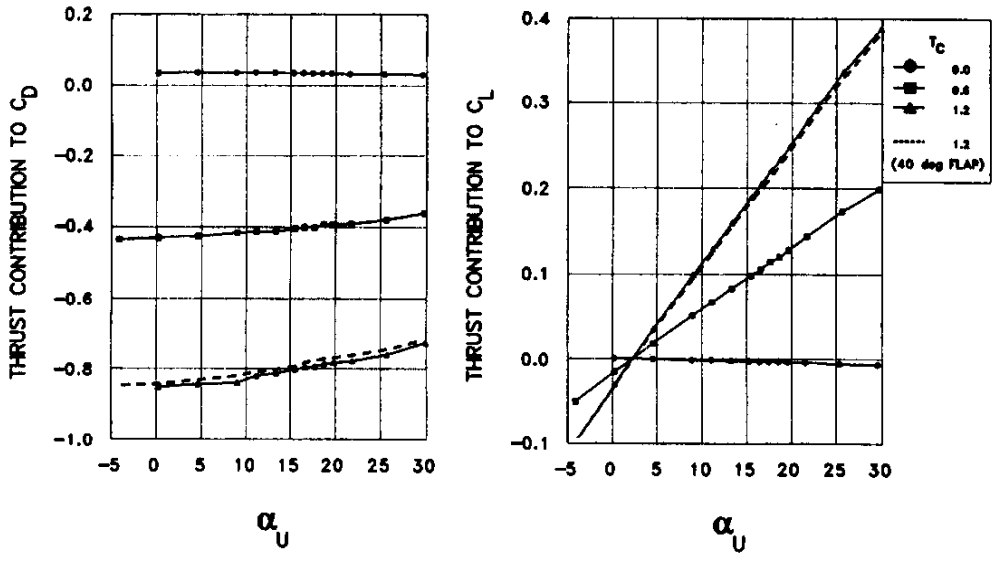

Figure 7.24 Thrust components to be removed from C_L and C_D

In the present zero-yaw cases the propeller-axis force is resolved into lift and drag using only angle-of-attack (Step (5)). Figure 7.24 shows re-normalised propeller thrust resolved into lift and drag components for all the cases considered. A loss in thrust component may be seen when high power is combined with high angle-of- attack (left plot, lowest curve). This reflects the loss of thrust seen under high-α, high thrust conditions in Figure 7.22. Finally, we see in Figure 7.25 the effect of removing the propeller forces from the measured values in Step (7). The left plot shows as-measured data; the right plot shows data with thrust components removed. No tunnel corrections have been applied. Neither the lift nor the drag curves in Figure 7.25 collapse to a single line. There is residual lift, increasing with thrust coefficient, that is probably slipstream-induced on the inner wing. There is also increased drag at high thrust settings. This

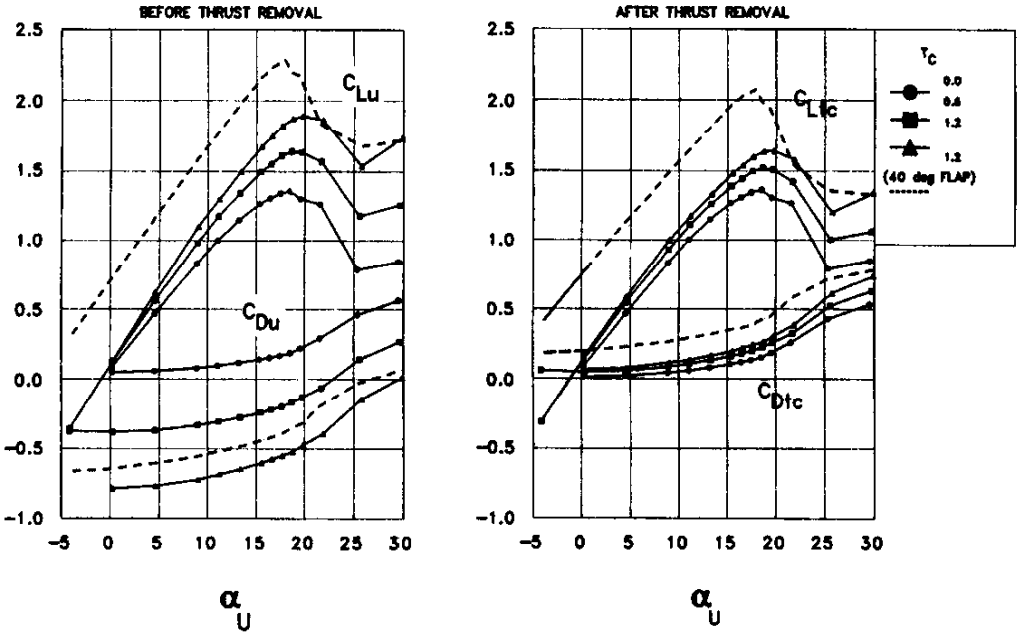

Figure 7.25 Effect of removing thrust components from measured C_L and C_D

certainly includes increased fuselage scrubbing drag and there is probably a vortex drag contribution, associated with slipstream-induced lift. We shall comment on this further in Section 7.4.4.

7.4.3.4 DISCUSSION

The above procedure is one of the simplest possible and so has some shortcomings. Since all data are referred to the model reference point, gradients in tunnel blockage and induced upwash result in conditions at the propeller (advance ratio, off-axis angle) that do not match those that would occur in free air. Consequently, the forces and moments on the propeller are also mismatched, which is why the propeller forces and moments are accounted separately. The mismatched propeller forces and moments are removed properly by the above procedure but the thrust level experienced by the propeller will be different from that in free flight. Consequently, the velocities within the slipstream, the scrubbing drag and any slipstream-induced lift will be slightly in error. These effects are usually secondary and errors in them are not likely to be important. Possible exceptions include situations in which slipstream-generated lift is used to enhance STOL capability, for example. More complicated test equipment and procedures (prop balances, near real-time blade angle tuning, etc.) may be needed in such cases.

7.4.4. APPLICATION OF TUNNEL CONSTRAINT CORRECTIONS

7.4.4.1 AIRFRAME FORCE AND MOMENT CORRECTIONS.

The principal feature that is observed with a propeller operating is the slipstream-induced loads (e.g., Figure 7.25). These will be of particular concern in cases where strong, slipstream-generated lift is present, as on some STOL aircraft. Shevell [13] gives the following description:

> "...the total lift consists of the lift from the wing without engine operation, the lift due to deflecting the exhaust stream downward and the additional circulation lift created by the action of the slipstream on the wing and flap system. The additional lift is called powered circulation lift. The physical basis of the latter can be the increased velocity over the wing and/or a larger effective flap chord created by the high-speed exhaust flow roughly parallel to and in the same plane as the flap chord."

The powered circulation lift, described above, is equivalent to a horseshoe vortex, spanning the slipstream at the appropriate chordwise position and carrying the appropriate lift. A further horseshoe vortex may be required to carry slipstream-induced lift on a flap. There is also an increase in wing/flap skin friction that can be represented by introducing a line source across the span involved.

When calculating bound vortex or source strengths for standard constraint corrections, it is usually assumed that a given load is generated at mainstream velocity. However, the flow is accelerated within a slipstream and has higher than mainstream total pressure. The standard procedure will overestimate the singularity strengths in this situation and the tunnel interference will be overestimated. Two alternative procedures will be described that address this.

Kupper [9] gives an analysis of slipstream effects and their correction for a twin engined configuration with wing-mounted nacelles. His analysis is very detailed and slipstream-on-tail effects, for example, are included[4]. Kupper starts by estimating the area of the wing wetted by the slipstream and the local dynamic pressure there. He then determines the power-dependent force and moment coefficient

[4]Kupper does not indicate, however, how the slipstream trajectory and its intersection with the tail is determined

increments and re-scales them by the ratio of mainstream-to-slipstream dynamic pressure. These increments are used to form new power-on coefficients of reduced magnitude, to which tunnel corrections are applied. The principal effect of Kupper's procedure appears to be a reduced correction to angle-of-attack.
The second treatment of slipstream-induced forces parallels the kinematic description of the flow given above. Pressure signature-based corrections to airframe loads are obtained as follows:

(1) Estimate the slipstream-induced forces, using the modelling techniques described above or those given by Kupper.

(2) Estimate the corresponding (short-span) singularity strengths, recognising the increased velocity, within the slipstream, that acts on them.

(3) Calculate the velocities at the tunnel-wall orifice locations induced by the singularities found in (2), with their images. Subtract these velocities from the measured signatures.

(4) Calculate the effects at the model of the images of the singularities found in (2). This is the interference at the model associated with powered circulation and slipstream scrubbing drag.

(5) Process the adjusted pressure signatures, from (3), using standard procedures to obtain 'rest-of-model' interference at the model sensing points.

(6) Combine the interference velocities found in (4) and (5) and apply them as needed.

The relationship between the above approach and that of Kupper is not clear. The factoring of singularity strength is explicit in the treatment above and the use of short-span singularities to represent the slipstream-induced forces has some appeal. It is not obvious that this level of resolution is present in Kupper's approach.

7.4.4.2 PROPELLER FORCE AND MOMENT CORRECTIONS

Free-air propeller calibration data can, in principle, be combined directly with airframe-only data, obtained using the procedures of Section 7.4.3 and corrected as described above. It could therefore be argued that there is no need to retain propeller forces extracted from whole-model tests. Whether this is true depends on whether there are any significant "feed-forward" effects from the wing. For a wing-mounted tractor propeller, for example, bound vortex effects may increase the advance ratio above the wing and decrease the advance ratio below it. The propeller then experiences wing-induced pitching moment and other components. These may be evaluated by comparing propeller balance data with interference-free data obtained from a full, angle-dependent calibration (Section 7.4.2) using the procedure described below. This procedure may also be used to estimate propeller loads, without the need for a propeller balance, if feed-forward is small.

The 'ideal' (no feed-forward) loads on the propeller are found from the propeller calibration in Step (5) of the procedure of Section 7.4.3. This includes the effects of non-zero off-axis angles. The loads are already normalised on local, in-tunnel dynamic pressure and the moment centre is the model reference point. The steps still to be performed concern the reduced-J interaction effect, described at the end of Section 7.4.2, and conventional tunnel blockage and upwash corrections. A further possible correction, for streamwise tunnel gradient, is also described in Section 7.4.2. Whole-model gradients (e.g., Figure 7.21) should be employed when using this correction.

When correcting propeller forces to the free-air condition, it should be recalled that, by definition, the mainstream dynamic pressure at the propeller in free air equals that at the model reference point. It is not

modified by tunnel effects. It follows that, having corrected for the effect of incorrect advance ratio, the position error correction to dynamic pressure (Figure 7.23 and Step (6), above) should not be applied when calculating free-air force and moment coefficients[5]. However, conventional corrections for tunnel blockage and tunnel-induced upwash at the propeller location still apply. Whole-model blockage data (Figure 7.21) and the corresponding upwash data should be used for these corrections.

The above procedure may be summarised as follows :

(1) Find the 'ideal' (no feed-forward) loads on the propeller using the calibration at the in-tunnel advance ratio and inflow angle. (Step (5) of Section 7.4.3).

(2) Using the full propeller calibration, determine the loads corresponding to the tunnel-induced change in advance ratio, relative to the model reference position. Subtract these loads from those found in (1).

(3) Apply standard blockage and angle-of-attack corrections to the loads just obtained using blockage and upwash interference velocities at the propeller location.

A gradient correction may be applied to the propeller loads after Step (2), above (see Section 7.4.2, last paragraph). The u-gradient at the propeller location should be used.

REFERENCES FOR CHAPTER 7

[1] AGARD, 1984, "Aerodynamics and Acoustics of Propellers" AGARD-CP-366.

[2] Ashill, P.R. and Keating, R.F.A., 1988, "Calculation of tunnel wall interference from wall-pressure measurements" Aeronautical Journal, Vol. 92, No.911, pp.36-53.

[3] Bradbury, L. J. S., 1967, "Simple expressions for the spread of turbulent jets" Aero. Quart. 18, 2, 133-142.

[4] Cooper, K.R., Hackett, J.E., Wilsden, D.J., 1995, "Closed test section wind tunnel blockage corrections for road vehicles" SAE SP 1176, May 1995.

[5] Glauert, H., 1947, "The Elements of Aerofoil and Airscrew Theory" Cambridge University Press, 2nd ed., pp.199-207.

[6] Hackett, J. E., Wilsden, D. J., and Stevens, W. A., 1981, "A review of the wall pressure signature and other tunnel constraint correction methods for high angle of attack tests" AGARD-R-692.

[7] Hackett, J.E., 1996, " Tunnel Induced Gradients and Their Effect on Drag", AIAA Journal, Dec. 1996, pp 2575-2581

[8] He Dexin, Jiang Giuquing, 1986, "An investigation of wall effect corrections for wind turbine tests in CARDC low speed wind tunnel" China Aerodynamic Research and Development Center Report CARDC-86-1020. (Presented at European Wind Energy Association Conference and Exhibition, Rome, Italy, Oct., 1986)

[9] Kupper, A., 1992, "Wall Correction Method for Models with Propeller Induced Slipstream" Programme of Wind Tunnels and Wind Tunnel Test Techniques, European Forum, Southampton University.

[10] Kuchemann, D., and Weber, J., 1953, "Aerodynamics of Propulsion" London, McGraw-Hill.

[5]This applies to data from a propeller balance as well as to calibration based data. The ensuing tunnel corrections are the same in both cases.

[11] Mokry, M., 1995, "Evaluation of Blockage Interference on Propellers in a Perforated-Wall Wind Tunnel" Journal of Aircraft, Vol.32, No.5, pp.1079-1087.

[12] Rae, William H., and Pope, Alan, 1984, "Low-Speed Wind Tunnel Testing" New York, p 290

[13] Shevell, Richard S., 1980, "Fundamentals of Flight" Prentice-Hall, 1980, p 224.

[14] Wright, R.H., 1959, "The Effectiveness of the Transonic Wind Tunnel as a Device for Minimizing Tunnel-Boundary Interference for Model Tests at Transonic Speeds" AGARD Rept.294.

Appendix: glauert.c

```
/* Ratio of Uncorrected and Corrected Stream Velocities
  for a Propeller in a Solid-Wall Wind Tunnel (Glauert's Method) */


#include <stdio.h>
#include <stdlib.h>
#include <math.h>

double glauert(double alpha, double tau);

void main(void)
{
 double alpha, tau=0.0;
 printf("\nEnter Ap/C (blockage ratio): ");
 scanf("%lf", &alpha);
 while(tau > -0.5)
 {
  printf("\nEnter tau (thrust parameter): ");
  scanf("%lf", &tau);
  printf("\n V/Vc =  %f\n", glauert(alpha,tau));
 }
}

double glauert(double alpha, double tau)
{
 int iter;
 double lambda, x, sigma, sigma1, ds, f, tau1, dt, dt1=0.0;

 /* test of input parameters */
 if(alpha < 0.0 || alpha >= 1.0) return(0.0);
 if(tau <= -0.5 || tau > 10.0) return(0.0);
 if(fabs(tau) < 1.0E-6) return(1.0);

 /* free air condition */
 x = sqrt(1. +2.*tau);
 sigma = (x +1.)/(2.*x);
 sigma1 = sigma;

 /* iteration cycle */
 for(iter=1; iter<=100; iter++)
 {
```

```
    f = (1. -sigma)*(1. -alpha*sigma)/(sigma*pow((1. -alpha*sigma*sigma),2.));
    x = (1. +f)/(1. -f);
    lambda = 1. +(x -1.)*alpha*sigma*sigma -((2.*sigma -1.)*x -1.)/(2.*sigma);
    tau1 = (x +1.)*(x -1.)/(2.*lambda*lambda);
    dt = tau -tau1;
    if(fabs(dt) < 1.0E-6) return(lambda);
    if(iter == 1) ds = 0.01*sigma1;
    else ds = 0.20*dt1*(sigma -sigma1)/(dt -dt1);
    sigma1 = sigma;
    sigma = sigma -ds;
    dt1 = dt;
  }
  return(0.0);
}

/* Example

Enter Ap/C (blockage ratio): 0.15

Enter tau (thrust parameter): 2.0

 V/Vc = 1.074788

*/
```